# Nonlinear scattering and mode conversion of Lamb waves at breathing cracks: An efficient numerical approach

Yanfeng Shen[a,*], Carlos E.S. Cesnik[b]

[a] University of Michigan-Shanghai Jiao Tong University Joint Institute, Shanghai Jiao Tong University, Shanghai 200240, China
[b] Department of Aerospace Engineering, University of Michigan, Ann Arbor, MI 48109, USA

## ABSTRACT

This article presents an efficient numerical approach to the investigation of nonlinear scattering and mode conversion phenomena of Lamb waves as they interact with breathing cracks. A Local Interaction Simulation Approach (LISA) is adopted, which possesses the versatility to capture arbitrary damage profiles. The stick-slip contact dynamics is implemented in the LISA model via the penalty method, which captures the nonlinear interactions between Lamb waves and breathing cracks. The LISA framework achieves remarkable computational efficiency with its parallel implementation using Compute Unified Device Architecture (CUDA) executed on powerful GPUs. A small-size LISA model with absorbing boundaries is tailored for the purpose of extracting the Lamb wave scattering and mode conversion features. Due to the explicit parallel CUDA implementation and the small-size model setup, the computation is highly efficient. Numerical case studies on nonlinear scattering of Lamb waves from breathing cracks are given. Distinctive higher harmonic generation and selective mode conversion phenomena are presented using the complex-valued Wave Damage Interaction Coefficients (WDICs) containing both amplitude and phase information of the scattered wave field. The effect of oblique incident angle on nonlinear scattering phenomenon is investigated. The rough crack surface feature with initial openings and closures is also considered to better approximate fatigue cracks in practical engineering scenarios. In addition, the wave amplitude effect on the nonlinear scattering and mode conversion is studied. This research may provide guidelines for the effective design of sensor arrays utilizing nonlinear Lamb waves for fatigue crack detection.

## 1. Introduction

Guided wave based Nondestructive Evaluation (NDE) and Structural Health Monitoring (SHM) systems generally diagnose damage by detecting the scattered wave field. The effectiveness and sensitivity of a sensor array depends on whether it can receive sufficient damage-scattered wave energy at the sensing locations. Thus, it is important to understand the scattering features of ultrasonic guided waves from structural damage. There are several major aspects that may influence the sensing signals such as wave mode sensitivity, interrogation frequency effectiveness, scattering amplitude directionality, and mode conversions. In the meanwhile, nonlinear ultrasonic techniques are drawing increasing attention among the NDE and SHM community due to their desirable sensitivity to incipient fatigue cracks [1–3]. However, understanding the guided wave nonlinear scattering feature is a challenging task, because it not only involves the multimodal and dispersive characteristics of guided waves but also presents distinctive nonlinear phenomena such as higher harmonic generation and selective mode conversion.

The fundamentals of wave damage interactions have been investigated extensively via different approaches. Analytical formulations facilitate accurate and efficient solutions to understand the complex plate guided wave scattering phenomena. Norris and Vemula studied the scattering of flexural waves in thin plates using Kirchhoff and Mindlin plate theory [4,5]. Hinders et al. investigated Lamb wave scattering from a through-thickness hole with the Kane-Mindlin plate theory [6,7]. Grahn put forward a solution for the same problem using a 3D expansion approach based on the lowest order plate theory of extensional and flexural motion which is only accurate at low frequency ranges in thin plates [8]. Utilizing such a wave function expansion method and Born approximation for S0 and A0 modes, Wang and Chang obtained the solution of guided wave scattering from a cylindrical inhomogeneity and compared with experiments [9]. Cegla et al. made an extension to Grahn's approach by exploring the guided wave scattering features from a partial through-thickness circular hole and by conducting experimental validations [10]. Moreau et al. contributed to the state of the art by introducing the exact 3D elasticity solution for guided wave scattering from through-thickness and flat-bottom cavities with irregular shapes using the expansion and projection method [11,12]. Poddar and Giurgiutiu recently proposed the complex mode expansion exact Lamb wave solution for horizontal cracks and disbonds scattering problems [13]. Lee and Kim further extended the 3D exact solution to handle arbitrary shaped elastic inclusions by treating the damage profile as the combination of subscatterer cubes using the T-matrix method [14]. As mathematically accurate and computationally efficient as they are, the analytical solutions, however, are generally limited to

relatively simple damage profiles and linear scattering problems. For more complex scattering scenarios, numerical methods are often adopted, such as the finite element method (FEM) [15], boundary element method (BEM) [16,17], spectral element method (SEM) [18], and distributed point source method (DPSM) [19,20]. Velichko and Wilcox developed a highly efficient frequency domain small-size FEM technique, which allows the convenient study of ultrasonic scattering and mode conversion phenomena in bulk wave and plate guided waves from arbitrary shaped 3-D damage [21–24]. Moreau et al. further explored this technique and compared with analytical solutions of the scattering problems for irregular defects [25,26].

Nevertheless, the state of the art generally focused on the linear scattering and mode conversion phenomena of Lamb waves, while the nonlinear scattering patterns have only been attained for bulk wave problems. The nonlinear scattering patterns of bulk waves from closed cracks have been investigated using time domain boundary integral equation given by Hirose and the nonlinear spring analytical model given by Poznic and Pecorari [27,28]. A recent bulk wave scattering analysis contribution is from Blanloeuil et al. utilizing FEM and an extended analytical approach [29,30]. Although particular nonlinear scattering patterns and mode conversion phenomena of Lamb waves have not been systematically reported in existing literature, increasing efforts on the investigation of nonlinear interactions between Lamb waves and breathing cracks have been seen. On-going analytical research by Wang and Su is being conducted to model the Contact Acoustic Nonlinearity (CAN) during the nonlinear interactions between Lamb waves and a breathing crack [31,32]. Such topic has been attempted using FEM contact analysis, the implicit nonlinear solution scheme and intensively large matrix operations have been found to impose much computational burden during the analysis [33]. Recently, a number of efficient numerical modeling methods have been presented to simulate the nonlinear interactions between guided waves and breathing cracks. Hafezi and Kundu presented a series of studies on the peri-ultrasound modeling of linear and nonlinear guided wave propagation as well as their interaction with structural damage [34–36]. Radecki et al. reported a numerical technique using LISA framework and the spring model to study the nonlinear interactions between Lamb waves and the breathing cracks in plates [37]. He and Ng used a time-domain spectral finite element method for the modeling and analysis of nonlinear plate guided wave interaction with a breathing crack [38]. However, to the best of the authors' knowledge, the investigation of nonlinear scattering patterns and mode conversion features of Lamb waves at breathing cracks is still very limited.

This study presents an efficient numerical approach to the investigation of nonlinear scattering patterns and mode conversion phenomena of Lamb waves at breathing cracks. A Local Interaction Simulation Approach (LISA) is adopted to construct a small-size numerical model with absorbing boundary condition. The contact LISA model follows an explicit solving scheme and is parallelized by Compute Unified Device Architecture (CUDA) accelerated on powerful GPUs, achieving remarkable computational efficiency. The small-size LISA model and wave mode expansion functions enable the extraction of wave scattering and mode conversion features of each plate guided wave mode at both fundamental and superharmonic frequencies. After the introduction section, the fundamentals of contact LISA and its implementation are given, followed by the presentation of the small-size LISA model with absorbing boundaries tailored for the scattering study purpose. The Wave Damage Interaction Coefficients (WDICs) concept is then reviewed and further extended to consider all possible plate guided wave modes at the fundamental and superharmonic frequency components. The wave mode expansion formulation for obtaining the WDICs is illustrated. Numerical case studies on nonlinear scattering of Lamb waves from breathing cracks are given. Distinctive higher harmonic generation and selective mode conversion phenomena are presented. The effect of oblique incident angle on nonlinear scattering phenomenon is then investigated. The rough crack surface feature with

initial openings and closures is finally considered as an effort towards the close approximation of practical fatigue cracks. The wave amplitude effect on the nonlinear scattering and mode conversion is studied.

It is necessary to clarify that the WDIC concept is not new. It was first proposed by the author and Giurgiutiu for the investigation of linear interactions between Lamb waves and a corrosion type of damage [39]. Before the present study, the WDIC practice was confined within the fundamental plate guided wave modes (S0, A0, and SHS0), whereas the higher modes (S1, A1, SHA0, S2, A2, SHS1, etc.) have not been discussed. Furthermore, the previous endeavors all focused on the conventional linear scattering phenomena, where the mode conversion would only happen among the wave modes at the same frequency. Thus, one novel portrait of the current research is the extension of the WDIC capability to cover all possible plate guided wave modes across the fundamental and superharmonic frequencies for the investigation of nonlinear wave damage interactions. In addition, the WDIC extraction procedure in the previous research generally utilized the commercial FEM package and harmonic solution, whereas the current study employs the LISA framework and transient dynamic solution. Thus, the WDIC extraction procedure presented here is also different and new compared with the linear scattering analysis. Detailed rationale behind such a choice will be given in Section 3. Moreover, it is worth of mentioning again that to the best of the authors' knowledge, the superharmonic scattering patterns and selective mode conversion phenomena have not been presented in previous scattering research. Thus, the results shown in this paper is another novel contribution to the state of the art.

It should also be noted that this article presents the authors' first step of numerical investigation to analyze the nonlinear scattering pattern and mode conversion phenomena at fatigue cracks. It intends to share the efficient numerical modeling scheme and scattering mode directivity quantification approach in a systematic manner. Experimental investigations will be reported in a future paper.

## 2. Local interaction simulation approach with contact acoustic nonlinearity

LISA is a finite-difference based numerical simulation method. It approximates the partial differential elastodynamic wave equations with finite difference quotients in the discretized temporal and spatial domains. The coefficients in LISA iterative equations (IEs) depend only on the local physical material properties. The Sharp Interface Model (SIM) enforces the stress and displacement continuity between the neighboring computational cells and nodes. Therefore, changes of material properties in the cells surrounding a computational node can be captured through these coefficients, which enables LISA to handle heterogeneous materials. The final iterative equations determine the displacements of a certain node at current time step based on the displacements of its eighteen neighboring nodes at previous two time steps, i.e., at current time step, all the computational nodes are independent, which facilitates its readiness for massive parallelization. 1-D, 2-D, and 3-D LISA formulations were first developed for isotropic heterogeneous materials executed on Connection Machines [40–42]. LISA underwent considerable progress during the past decade, with its application in metallic structures [43,44], extension to general aniso-tropic materials [45–47], coupled field capabilities [48], hybridization with other numerical methods [49,50], and execution on powerful Graphics Processing Units (GPU) with Compute Unified Device Architecture (CUDA) technology [51–53].

In the authors' recent study, a penalty method was deployed to introduce contact dynamics into the LISA formulation to realize the simulation of CAN [54]. A Coulomb friction law was integrated into the model to capture the stick-slip contact motion. A distributed random gap function was applied on the crack surface to model the roughness of the contact interface with initial openings and closures. The comparative study with the conventional FEM simulations not only validated the

modeling accuracy but also demonstrated the superb computational efficiency of the LISA method. For detailed theoretical formulation, numerical algorithm, and case studies, readers are referred to Ref. [54]. The contact LISA algorithm was implemented using CUDA technology and executed in parallel on GPUs (NVIDIA GeForce Titan with 2688 CUDA cores and 28,672 concurrent threads). There are two major characteristics of the current contact LISA formulation that enables the computation to be expedited. First, the LISA algorithm is massively parallel. This is because the computation of a general node or a contact node only depends on the solutions of its eighteen neighboring nodes at the previous two time steps. Thus, the behavior of each node is independent from the others at the target time step, i.e., the computation of each node can be carried out individually in parallel. Second, the wave propagation simulation tasks usually require dense discretization of the structure, resulting in a computationally intensive problem. GPUs, with their massive concurrent thread feature, are suitable to handle such large size problems by distributing the workloads among a large number of functional units and carry out highly efficient parallel computing. During the computation, the parameters are first established in the host memory (RAM). Then a copy of these parameters is sent to the device memory (GPU global memory) for it to be processed. The computation of each node is assigned to a functional thread, i.e., each thread gathers the displacements of its eighteen neighboring nodes and one contact pair node (if identified as a contact node) at previous two time steps, process the material properties in the eight surrounding cells, and execute the kernel to compute the displacements of this node at the target time step. Since one of the bottlenecks of a CUDA program is the data transfer between the device memory and the host memory, results are transferred from the GPU to the CPU only sporadically (every 10–30 steps depending on the frequency of the propagating waves) to minimize such data transfer cost.

## 3. Small-size LISA model for studying Lamb wave scattering

Fig. 1 shows the small-size LISA model specially tailored for investigating wave damage interactions. The model consists of an interior damage region and an exterior absorbing boundary. It should be noted that the LISA model layout is similar to the small-size FE model proposed in Refs. [22,25]. However, the LISA formulation and the nonlinear contact transient analysis make the current approach stand out. The interior region is able to capture arbitrary damage profiles due to the versatile adaptiveness of the spatial discretization, while the exterior absorbing boundary would eliminate the boundary reflections. For this particular study, Absorbing Layers with Increasing Damping (ALID) is applied to implement the absorbing boundary. Thus, the simulation of guided wave scattering in an infinite plate can be achieved utilizing the small-size local LISA model. In general, the extended ALID region should be longer than twice the longest wavelength under consideration [55,56]. Overall, there are three factors contributing to the
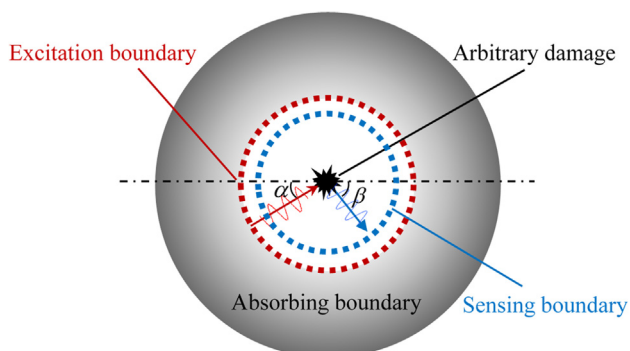


**Fig. 1.** Small-size LISA model with absorbing boundary condition for studying Lamb wave scattering from arbitrary damage types.

high computational efficiency of the approach: (1) LISA formulation with simple algebraic operations; (2) parallel computation using CUDA technology accelerated on powerful GPUs; and (3) computationally economical model size with absorbing boundaries.

The external red circle in the model shows the incident wave excitation locations, while the internal blue circle represents the scattering wave sensing locations. The circular-shape locations allow the investigation of scattered waves in an arbitrary direction $\beta$ from an incident wave with the arbitrary incident angle $\alpha$. At the wave generation locations, circular areas of out-of-plane traction forces are applied on both top and bottom surfaces of the plate. Anti-phase traction force pairs will generate symmetric Lamb wave mode (S0) and in-phase traction force pairs will generate anti-symmetric Lamb wave mode (A0). At the sensing locations, for each scattering direction $\beta$, a number of sensing points across the thickness at locations $Z_i$ are obtained for mode expansion analysis.

To obtain the scattered wave field, a pair of such small-size LISA model is needed: one pristine case and one damaged case. The pristine case model provides the wave field of the incident waves, while the damaged case gives the wave filed of the total waves, i.e., the superposition of incident waves and scattered waves. The subtraction of incident waves from the total wave field renders the scattered wave field. It should be pointed out that the model described in Ref. [22] allows the extraction of all scattering information from only one FE analysis. In this research, however, the small-size LISA procedure was tailored to obtain the relative relationship of amplitude and phase between a certain incident wave mode and the scattered wave modes. This is especially beneficial when these scattering features enter a global analytical solution as input parameters [57,39].

It should be noted that the prevailing practice of studying Lamb wave scattering phenomena generally builds upon the harmonic analysis using standard FEM codes for the numerical solution [25,39]. However, such type of analysis is only feasible for linear problems; on the other hand, it is more appropriate to handle CAN with time-historic solutions, which is the reason why transient analysis is adopted in the current study. Although both FEM and LISA can provide accurate simulation results for such a purpose, the explicit parallel LISA formulation has demonstrated considerably superior computational efficiency than FEM which usually involves the operation of large matrices and iterative converging schemes for nonlinear solutions. Thus, to ensure the analysis efficiency, LISA is adopted instead of FEM. It should be emphasized that the current paper does not aim to compare the results between FEM and LISA solutions. As a matter of fact, the accuracy and computational efficiency of the nonlinear LISA solution has been checked and proved against commercial FEM packages in the authors' previous research [54].

## 4. Formulation for quantitative evaluation of scattered wave modes

This section presents the special consideration for multimodal Lamb waves and the wave mode expansion formulation to extract the complex-valued WDICs for the quantitative evaluation of Lamb wave scattering and mode conversion. The challenges raised by multimodal plate guided waves at higher harmonic frequencies are discussed. Fundamental theory and detailed formulation for WDICs are given.

### 4.1. Consideration for multimodal plate guided waves

Mode conversion phenomena have been widely reported in the existing literatures, i.e., a certain incident wave mode may be converted to other possible wave modes during the Lamb wave scattering procedure. In the context of nonlinear scattering, the mode conversion phenomena can be further complicated by the well-known nonlinear higher harmonic generation effect, i.e., an incident wave centered at the fundamental frequency will introduce response at the integer multiple
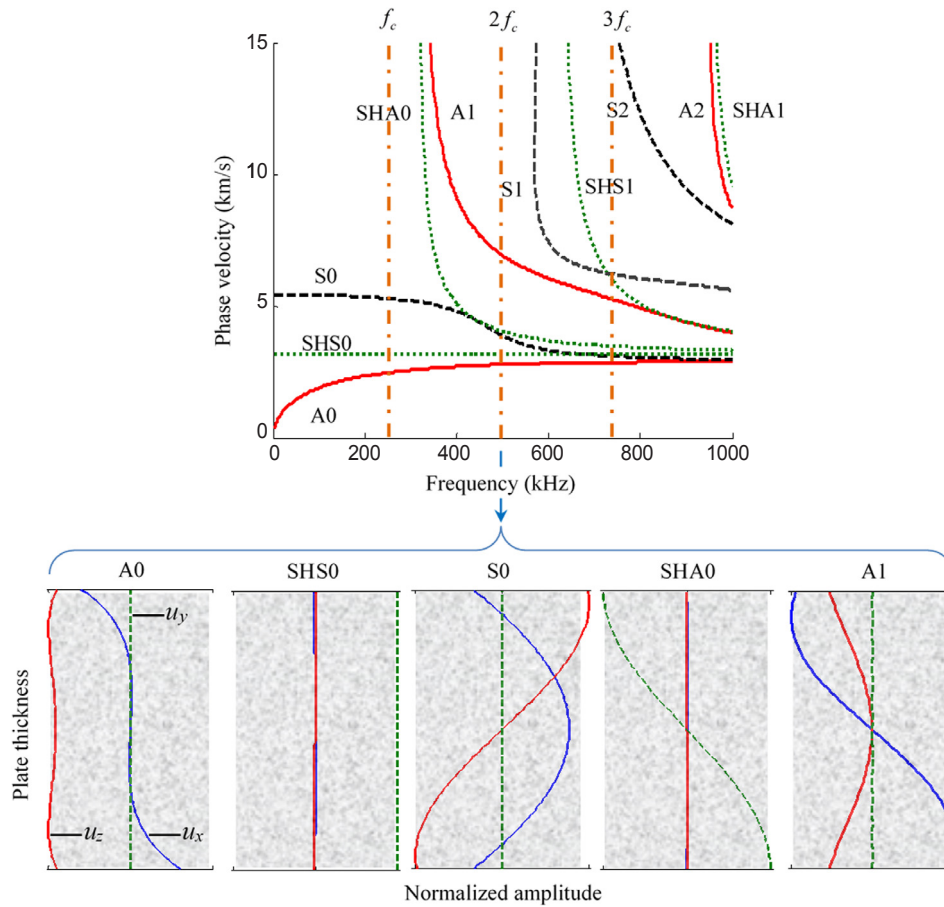
**Fig. 2.** Multi-modal plate guided waves and their mode shapes at the second harmonic frequency for a 5-mm thick aluminum plate.

frequencies of the fundamental component in the scattered wave field. The frequency components beyond the cut-off frequencies will introduce, in theory, an infinite number of wave modes in the scattered wave field. Thus, the consideration for multimodal nature of the guided waves is one of the major challenges during the analysis.

Fig. 2 shows the dispersion curves of plate guided waves in a 5-mm thick aluminum plate. In order to capture the scattering wave features, all the plate guided wave modes should be considered in the scattering analysis, because one incident wave mode may be converted to all possible Lamb modes and shear horizontal (SH) modes. For instance, a 250-kHz excitation may result in frequency components at 250 kHz, 500 kHz, 750 kHz, etc. in the scattered wave field. These higher harmonic frequencies will inevitably bring in an increasing number of higher order Lamb modes and shear horizontal (SH) modes when higher harmonics appear beyond corresponding cut-off frequencies. The increasing number of wave modes will result in multiplex possibilities of mode conversions. It can be observed that, at the fundamental frequency $f_c$ (250 kHz), there are three fundamental wave modes: A0, SH-S0, and S0. Thus, a certain type of incident wave mode can be converted to any of these three wave modes after interacting with the damage. However, at $2f_c$ (500 kHz), there are five possible wave modes: three fundamental modes (A0, SH-S0, S0) and two higher order modes (SH-A0 and A1). Thus, one incident wave mode may be converted into all these five possible wave modes. Fig. 2 also presents the five plate wave mode shapes at the second harmonic frequency. These mode shapes will be used to achieve the mode expansion for the quantitate evaluation of scattered waves.

### 4.2. Wave damage interaction coefficients extraction

The quantitative participation of each wave mode in the scattered

wave field is represented by the wave damage interaction coefficients (WDICs) $C_{IN-N}(\alpha, \beta, f_n)$. The two sub-indices are used to designate the incident wave mode ($IN$) and the scattered wave mode ($N$), respectively. $\alpha$ and $\beta$ are the incident angle and scattered direction as given in Fig. 1. $f_n$ represents the harmonic frequency component, i.e., $f_1$ represents fundamental excitation frequency, while $f_2$ and $f_3$ represents second and third higher harmonic frequencies, respectively. For instance, $C_{S0-SHS0}(20, 30, f_2)$ represents the scattering coefficient of S0 wave with 20° incident angle and mode converted to SHS0 in the 30° scattered direction at the second harmonic frequency. Thus, the WDICs can capture the mode conversion and higher harmonic generation phenomena.

The extraction of WDICs from the small-size LISA model can be realized in the following steps:

STEP 1: after the computation of a pristine case (incident wave field $u_{IN}$) and a damaged case (total wave field $u_{Total}$), the scattered wave field is obtained by

$$u_{SC} = u_{Total} - u_{IN} \tag{1}$$

STEP 2: the scattered wave field at the sensing boundary is evaluated using the cylindrical coordinate system shown in Fig. 3 through coordinate transformation. $u_r(\beta, t, Z_i)$, $u_\theta(\beta, t, Z_i)$, and $u_z(\beta, t, Z_i)$ represent the cylindrical coordinate displacements of the scattered wave field at various thickness locations $Z_i$ in the scattering direction $\beta$. It should be noted that, in the pristine case, an additional center sensing node is used. The displacements in the center of the model are recorded as the incident wave field impinging on the damage location $u_{IN}^{Center}(\alpha, t)$. It will be used to construct both the amplitude and phase relationship between the
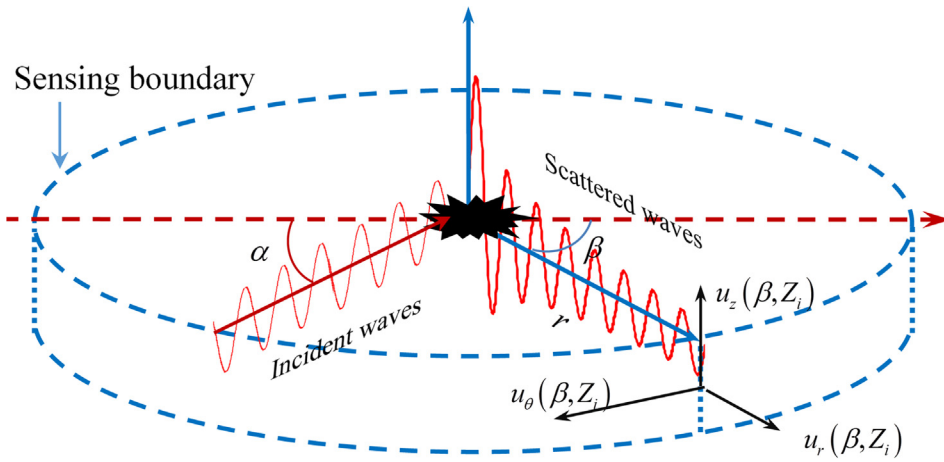
**Fig. 3.** Cylindrical coordinate system and the sensing points in an arbitrary scattering direction $\beta$ through the plate thickness.
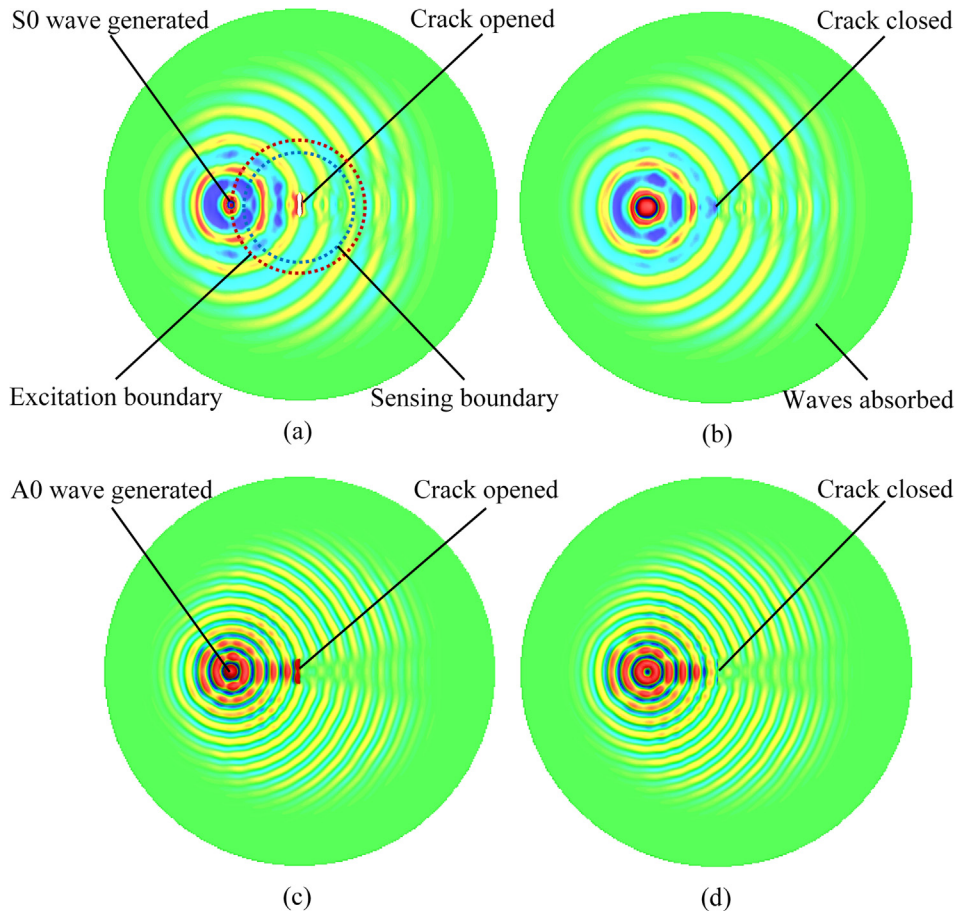


**Fig. 4.** Small-size LISA model simulation results: (a) S0 wave opened the crack; (b) S0 wave closed the crack; (c) A0 wave opened the crack; (d) A0 wave closed the crack.

incident and scattered wave fields.

STEP 3: both the incident wave impinging on the damage location and the scattered waves at the sensing locations are Fourier transformed into frequency domain.

$$U_{SC}^{LISA}(\beta, f_n, Z_i) = FFT\left[u_{SC}^{LISA}(\beta, t, Z_i)\right] \quad (2)$$

$$U_{IN}^{Center}(\alpha, f_1) = FFT\left[u_{IN}^{Center}(\alpha, t)\right] \quad (3)$$

STEP 4: consider the waves irradiating from a localized source follows the solution of Hankel functions [20,39], forming the outspreading propagation pattern. The plate guided waves scattered

from a small-size damage is assumed to take such a solution format. The wave scattering formulation in terms of mode expansion can be written as

$$\sum_N u_{IN}^{Center}(\alpha, f_1) \cdot C_{IN-N}(\alpha, \beta, f_n) \cdot \phi_N(f_n, Z_i) \cdot H_m^{(1)}(\xi_N r) \cdot e^{-i\omega_n t}$$

$$= U_{SC}^{LISA}(\beta, f_n, Z_i) \cdot e^{-i\omega_n t} \quad (4)$$

where $\xi_N$ is the frequency dependent wavenumber of wave mode $N$; $\phi_N(f_n, Z_i)$ represents the corresponding mode shapes at harmonic frequency $f_n$ (corresponding to the angular frequency $\omega_n$) at the thickness location $Z_i$. $H_m^{(1)}$ is the Hankel function of the first kind and order $m$. For
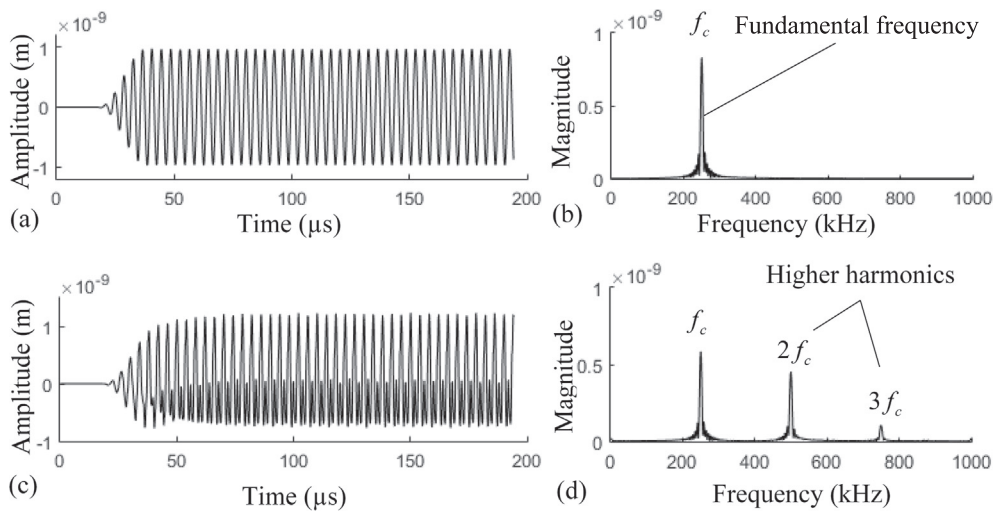
Fig. 5. Signal examples: (a) time trace of excitation signal; (b) frequency spectrum of excitation signal; (c) time trace of scattered signal (note the heavy distortion of waveform); (d) frequency spectrum of scattered signal (note the generation of higher harmonics).
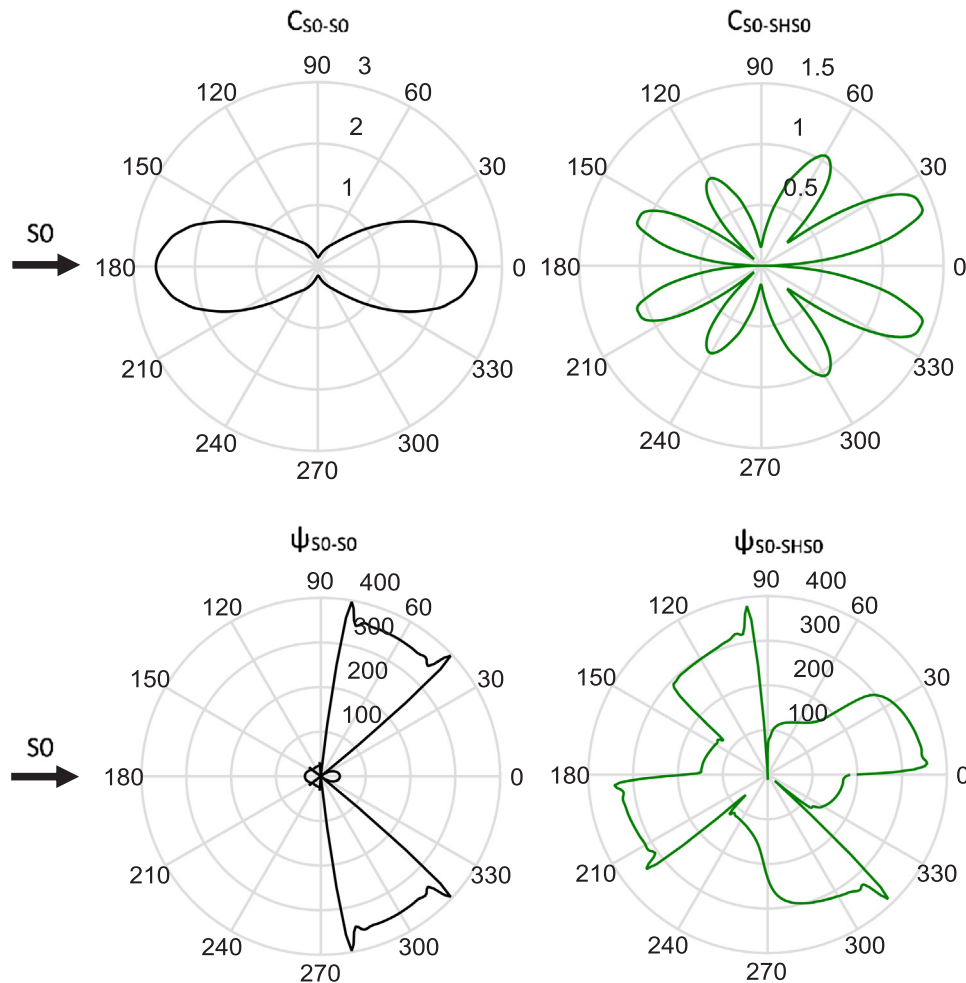


Fig. 6. WDICs for S0 incident wave at the fundamental frequency f1 (250 kHz). Note: mode conversion does not happen between incident S0 mode and A0 mode, i.e., no S0 wave is converted to A0 wave at the breathing crack.

Lamb waves, $m = 1$; for SH wave, $m = 0$. $r$ is the distance from the center of the model to the sensing boundary. $i = \sqrt{-1}$ is the unit imaginary number. The physical interpretation of Eq. (4) is that the waves impinging on the damage is scattered according to the WDICs governing the participation of each scattered wave mode. These scattered waves carry their corresponding mode shapes, undergo an out-spreading propagation pattern, and finally arrive at the sensing boundary, i.e., the scattered wave field at the sensing boundary is the superposition of all the possible wave modes in the form of mode expansion; the WDICs relates the amplitude and phase of the incident
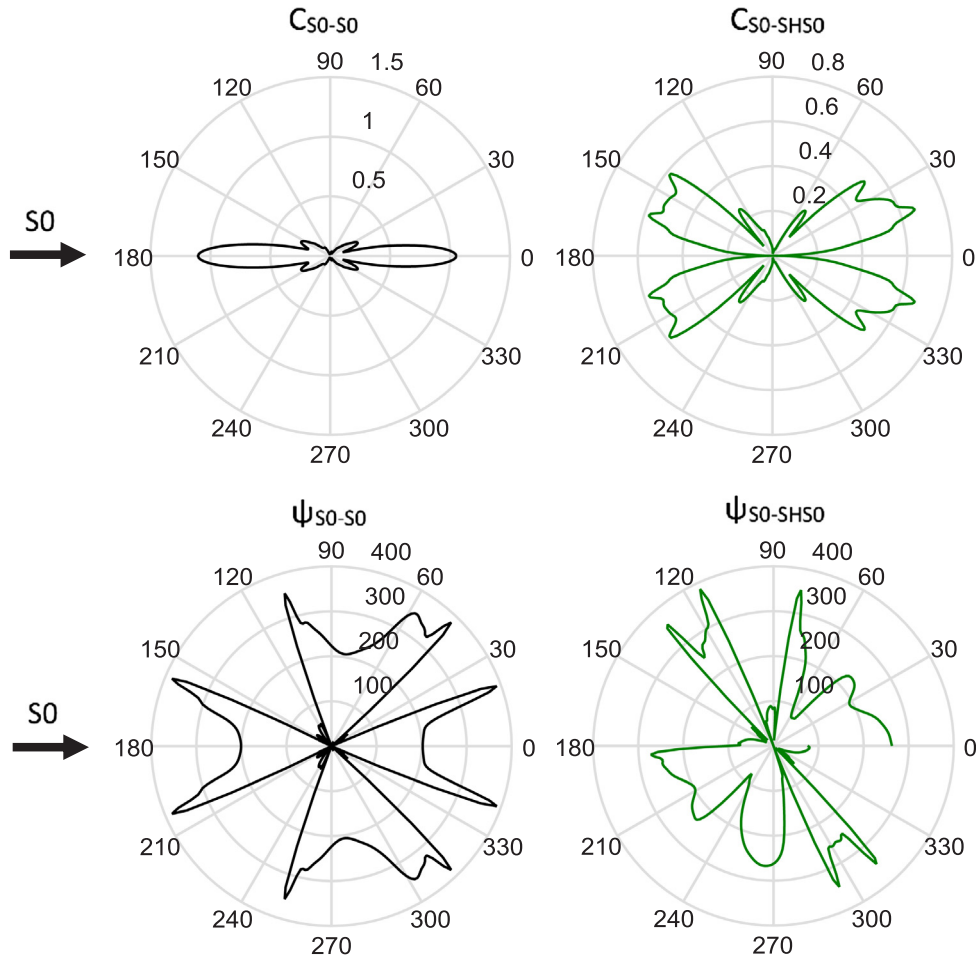
**Fig. 7.** WDICs for S0 incident wave at the second harmonic frequency f2 (500 kHz). Note: mode conversion does not happen from incident S0 wave to A0, SHA0, or A1 modes.

wave with the scattered waves at the damage location.

The incident wave $u_{IN}^{Center}(\alpha, f_1)$ and scattered sensing signals $U_{SC}^{LISA}(\beta, f_n, Z_i)$ have been obtained as complex numbers from the Fourier transform in Step 3. The mode shapes $\phi_N(f_n, Z_i)$ and wavenumbers $\xi_N$ can be obtained from either the analytical solution or the Semi-analytical Finite Element (SAFE) method. The only unknown terms in Eq. (4) are the WDICs. Note that Eq. (4) will provide an independent equation for each sensing node along each cylindrical coordinate direction. For instance, if $n$ nodes across the thickness are used, then a total of $3n$ independent equations will be obtained for a certain scattering direction. In the end, one arrives at an over-determined system of equations with fixed number of unknown WDICs for a certain frequency and a large number of equations depending on the number of solution points used across the thickness.

STEP 5: In order to implement the WDIC extraction procedure, Eq. (4) can be casted into matrix form and solved using the least square method, i.e.,

$$\Phi_{3n \times N} \cdot H_{N \times N} \cdot C_{N \times 1} = \frac{1}{U_{IN}^{Center}} U_{SC\_3n \times 1}^{LISA} \tag{5}$$

where $\Phi$ is the mode shape matrix; $H$ is the Hankel function diagonal matrix; $C$ is the WDIC vector; $U_{SC}^{LISA}$ is the LISA solution vector. These matrices are given as:

$$\Phi = \begin{bmatrix} \phi_1^r(Z_1) & \phi_2^r(Z_1) & \cdots & \phi_N^r(Z_1) \\ \vdots & \vdots & & \\ \phi_1^r(Z_i) & \phi_2^r(Z_i) & \cdots & \phi_N^r(Z_i) \\ \phi_1^\theta(Z_1) & \phi_2^\theta(Z_1) & \cdots & \phi_N^\theta(Z_1) \\ \vdots & \vdots & & \\ \phi_1^\theta(Z_i) & \phi_2^\theta(Z_i) & \cdots & \phi_N^\theta(Z_i) \\ \phi_1^z(Z_1) & \phi_2^z(Z_1) & \cdots & \phi_N^z(Z_1) \\ \vdots & \vdots & \vdots & \\ \phi_1^z(Z_i) & \phi_2^z(Z_i) & \cdots & \phi_N^z(Z_i) \end{bmatrix} \tag{6}$$

$$H = \begin{bmatrix} H_m^{(1)}(\xi_1 r) & 0 & \cdots & 0 \\ 0 & H_m^{(1)}(\xi_2 r) & 0 & \vdots \\ \vdots & 0 & \vdots & 0 \\ 0 & \cdots & 0 & H_m^{(1)}(\xi_N r) \end{bmatrix} \tag{7}$$

$$C = [C_1 \quad C_2 \quad \cdots \quad C_N]^T \tag{8}$$

$$U_{SC}^{LISA} = [U_r^{LISA}(Z_{1 \to i}) \quad U_\theta^{LISA}(Z_{1 \to i}) \quad U_z^{LISA}(Z_{1 \to i})]^T \tag{9}$$

The solution of Eq. (5) is conducted for each scattering direction and the final direction-dependent scattering WDICs are obtained. The WDICs are complex-valued coefficients which contain corresponding amplitude and phase information. The phase coefficients can be evaluated on $[0, 2\pi]$.
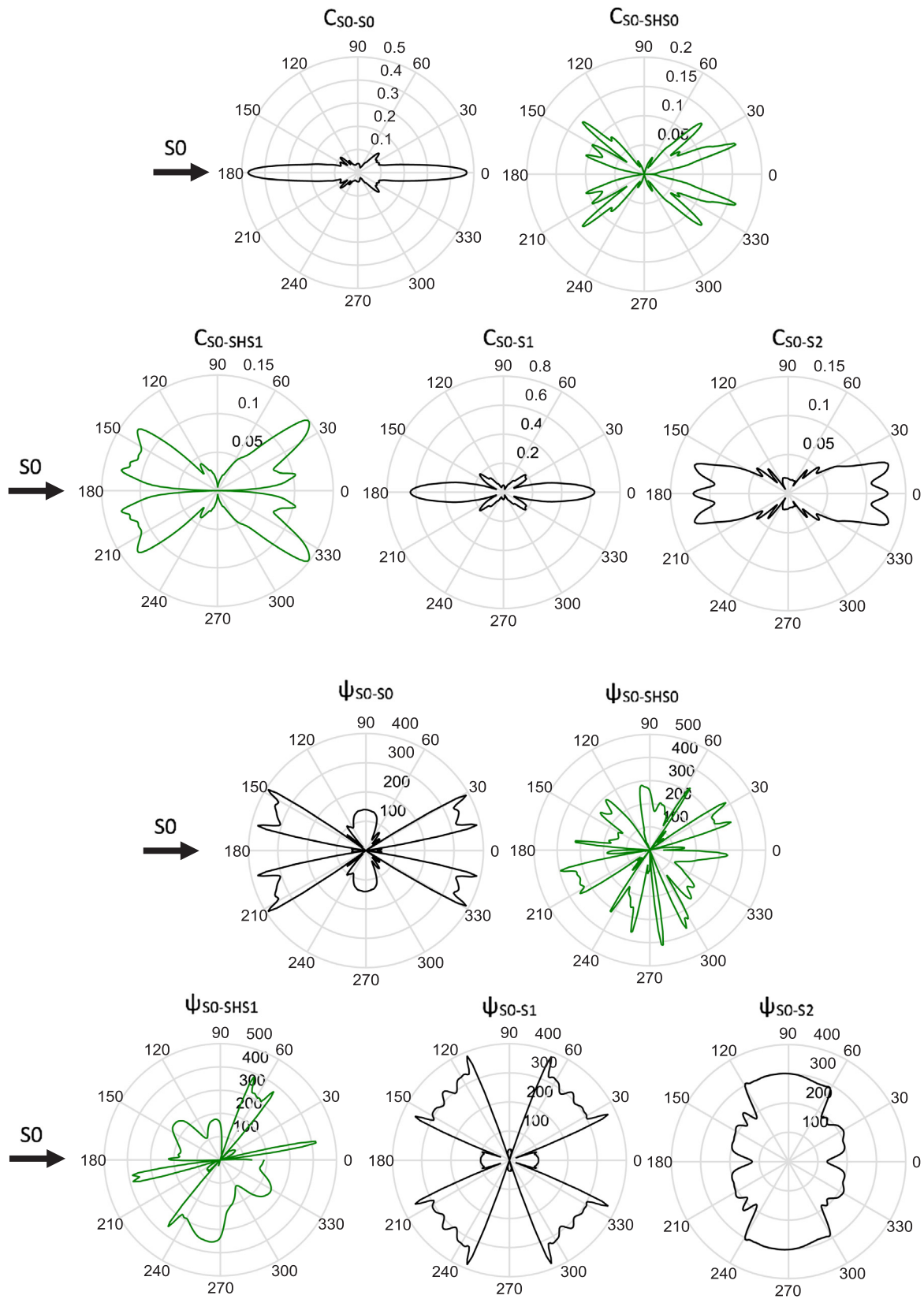
**Fig. 8.** WDICs for S0 incident wave at the third harmonic frequency f3 (750 kHz). Note: mode conversion does not happen from incident S0 mode to A0, SHA0, and A1 modes. S0 mode was scattered as the symmetric modes (S0, SHS0, SHS1, S1, and S2).
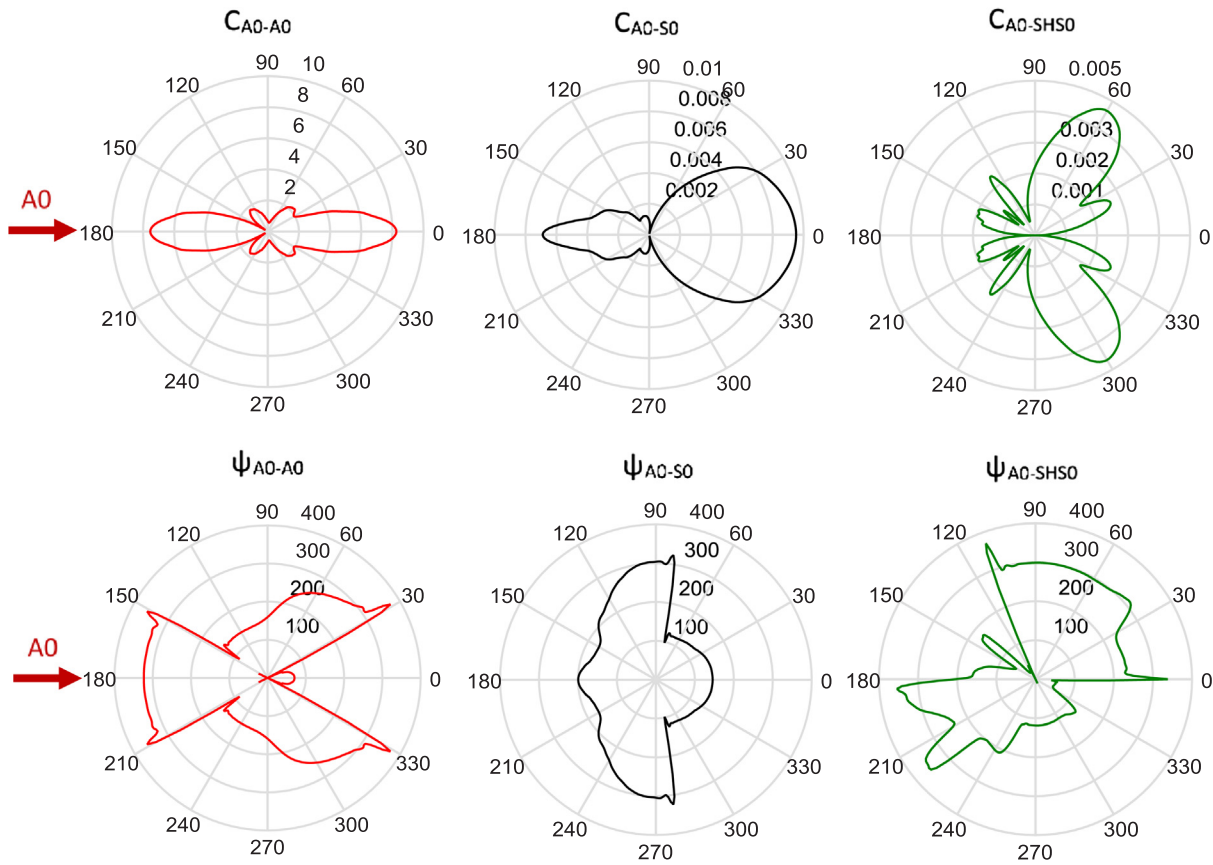
**Fig. 9.** WDICs for A0 incident wave at the fundamental frequency f1 (250 kHz). Note: all possible wave modes participate in the scattering procedure.

## 5. Nonlinear scattering and mode conversion

This section will present the case study of Lamb wave scattering and mode conversion from a through-thickness breathing crack. Simulation results and example signals are presented. The scattering and mode conversion features of the fundamental Lamb wave modes S0 and A0 are discussed in detail.

### 5.1. Case study

Fig. 4 shows the simulation results for a case study of the nonlinear interaction between fundamental guided wave modes and a 2-cm long through-thickness crack in a 5-mm thick aluminum plate. This case simulates the normal incidence of guided waves to the straight line crack. Selective S0 and A0 Lamb modes are generated by continuous harmonic surface traction forces at 250 kHz.

To accommodate all the possible wave modes participating in the scattering procedure, the model size is set to be 100 mm in radius. And the wave generation location is 50 mm away from the crack at the center of the model. The sensing circle has a radius of 40 mm (8 times the plate thickness), which allows the complete development of propagating wave modes and excluding the influence from the evanescent modes. Thus, at the sensing locations, only propagating modes meaningful for SHM systems will be picked up. The absorbing region extends from the excitation locations with a coverage length of 50 mm. The LISA models used in this study adopts the in-plane cell size of 1 mm and a through-thickness cell size of 0.5 mm. The time step according to the Courant-Friedrichs-Lewy (CFL) condition is 64.75 ns, which corresponds to a CFL number of 0.99.

Fig. 4a and b present S0 wave interaction with the breathing crack, while Fig. 4c and d show A0 wave interaction with the breathing crack. The crack open and close phenomena can be clearly noticed for both S0

and A0 cases. Such crack open-close contact-impact mechanism gives rise to the nonlinearity in the sensing signals. It can be observed that the waves which entered the ALID region are effectively absorbed.

Fig. 5a shows the time trace of the excitation signal. A half Hanning window is applied on the continuous harmonic sine wave to smoothly introduce guided waves into the dynamic system. Fig. 5b presents the frequency spectrum of the excitation signal with only one component $f_c$ at the fundamental excitation frequency (250 kHz). Fig. 5c shows the out-of-plane component $u_Z$ of the scattered wave signal during S0 wave interaction with the breathing crack. The scattered signal is heavily distorted with obvious zigzag shapes. Fig. 5d presents the frequency spectrum of the scattered wave signal. It can be observed that in addition to the fundamental frequency $f_c$, distinctive higher harmonic components at $2f_c$ and $3f_c$ are present.

The following subsections present the WDIC results for the 5-mm thick aluminum plate with a 2-cm long breathing crack. The case study focuses on two fundamental incident wave modes: S0 and A0, both impinging perpendicularly on the crack surfaces ($\alpha = 0$).

### 5.2. S0 mode nonlinear scattering

Fig. 6 shows the WDICs for the S0 incident wave at the fundamental frequency $f_1$ (250 kHz). The first row presents the amplitude coefficients, while the second row presents the phase coefficients. At the excitation frequency, only three fundamental wave modes (S0, SHS0, and A0) exist. After interacting with the breathing crack, it was found that the S0 waves were not converted to A0 mode, since the WDIC of $C_{S0-A0}$ has an order of magnitude around $10^{-10}$. Hence, the coefficients associated with mode conversion from S0 into A0 are not plotted for the sake of clarity and brevity. The S0 wave is scattered in its own mode type as shown by the $C_{S0-S0}$ coefficient. Along the incident direction, the scattered S0 wave possesses the largest scattering amplitude, which
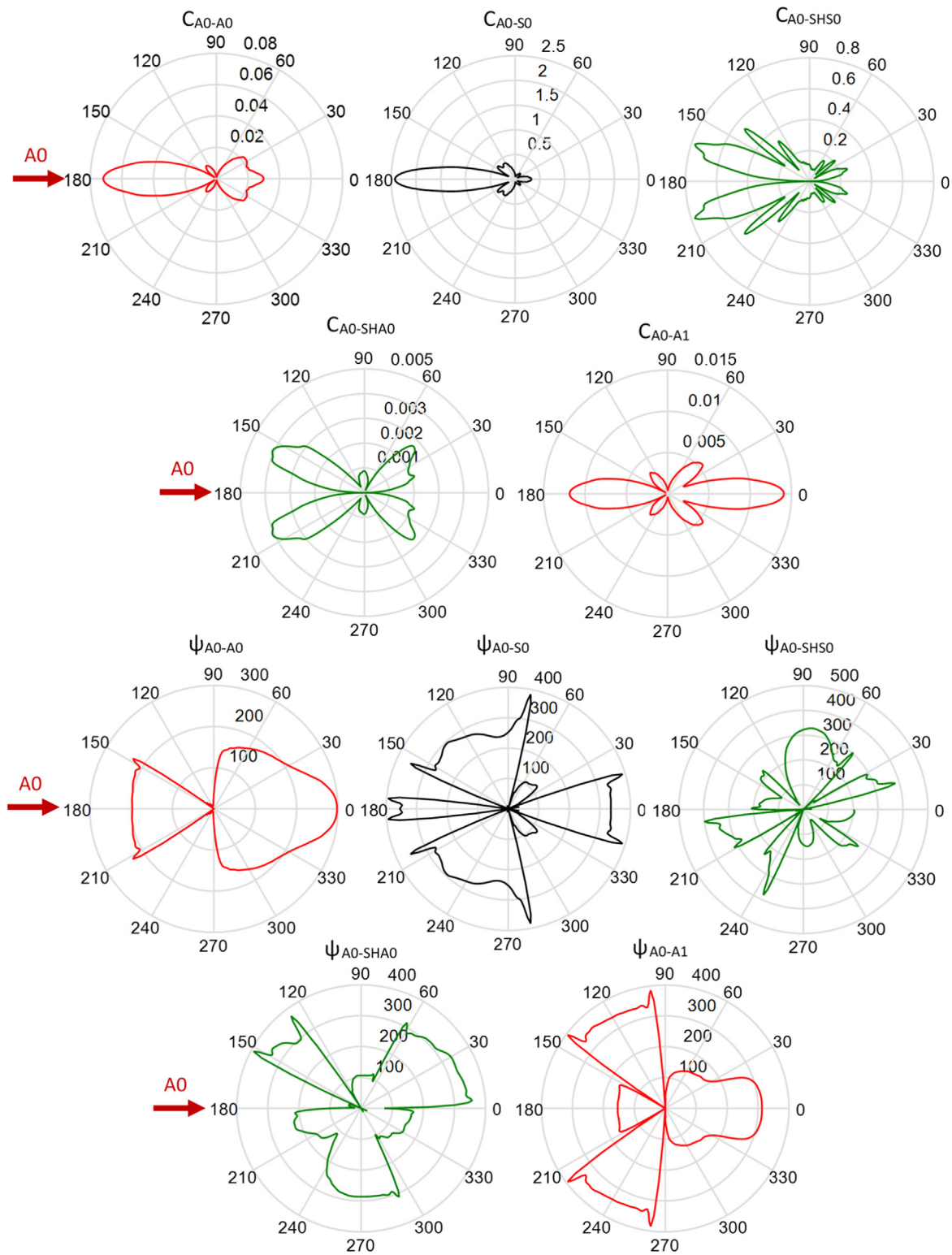
**Fig. 10.** WDICs for A0 incident wave at second harmonic frequency f2 (500 kHz). Note: all possible wave modes participate in the scattering procedure.

indicates that to detect the scattered wave, the most effective location to place the sensors is along the wave path. Mode conversion takes place between the incident S0 mode and the scattered SHS0 mode. The highest SHS0 scattering amplitude peaks appear around ± 25° and ± 60°.

Fig. 7 shows the WDICs for the S0 incident wave at the second harmonic frequency (500 kHz). At this frequency, a total number of five wave modes exist: A0, S0, SHS0, SHA0, and A1. Based on the WDIC

amplitudes, the S0 wave mode was not converted to any of A0, SHA0, or A1 modes. Only S0 and SHS0 mode component exist in the scattered wave field. The scattered S0 wave amplitude shows more concentrated directionality along the wave path direction. For SHS0, the scattered amplitude focuses along ± 20°.

Fig. 8 presents the WDICs for the S0 incident wave at the third harmonic frequency (750 kHz). A total number of eight wave modes may exist. The result shows that only five wave modes participated in
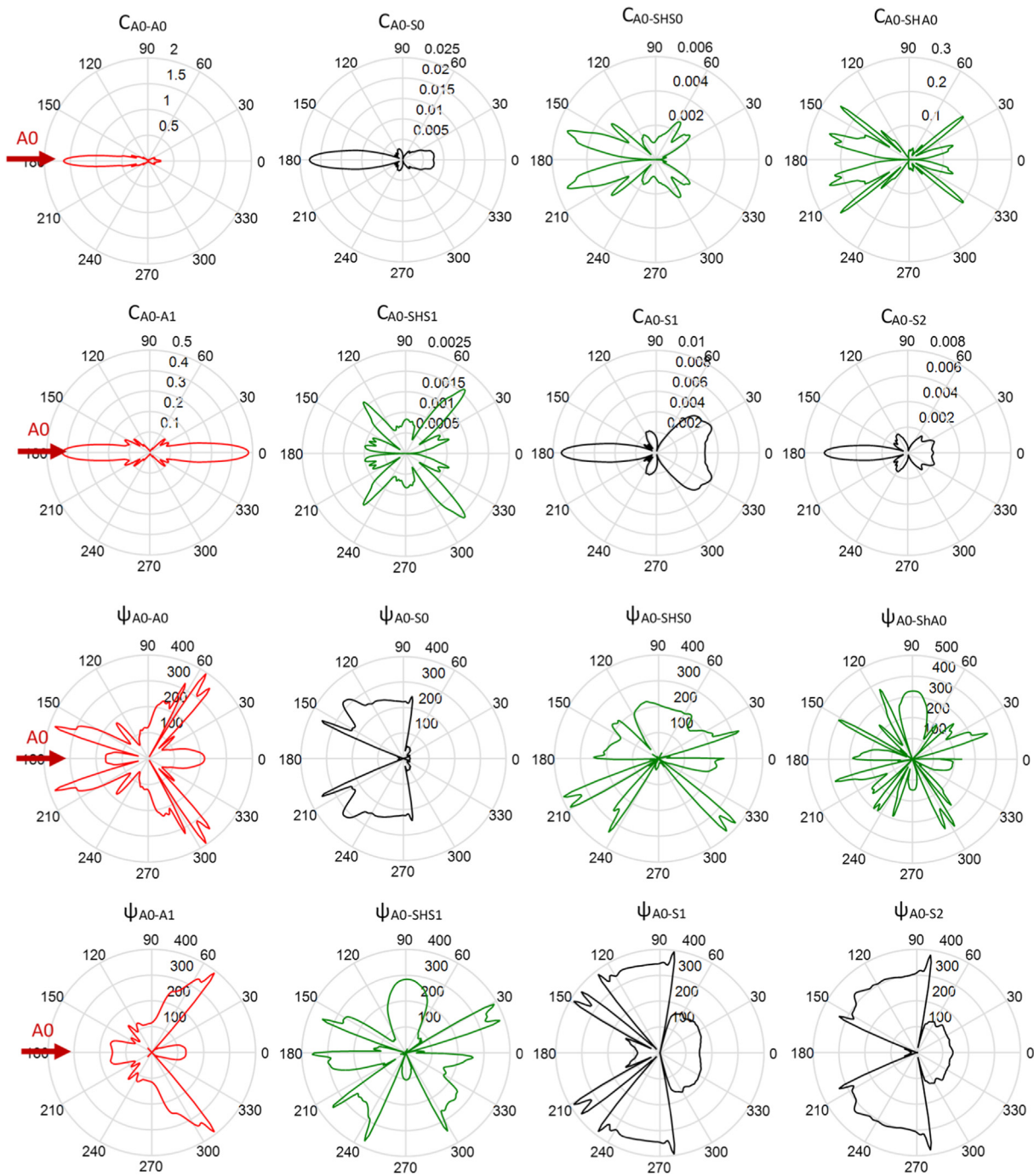
**Fig. 11.** WDICs for A0 incident wave at third harmonic frequency f3 (750 kHz). Note: all possible wave modes participate in the scattering procedure.

the scattering procedure: S0, SHS0, SHS1, S1, and S2. It can be noticed that all the scattered S0, S1, S2 modes have the highest amplitude along the wave path direction, whereas SHS0 mode showed the highest scattering amplitude along ± 20° and SHS1 mode along ± 45°. Thus, the results presented in Figs. 7 and 8 indicate that for nonlinear ultrasonic SHM and NDE techniques, to pick up the second and third higher harmonic components, conventional Lamb wave sensors should be placed along the wave path direction, whereas SH sensors should be placed off the propagation axis. The shear horizontal modes are converted from the wave damage interaction and scattered in the off-axis directions. Finally, the phase coefficients are important because they govern the constructive or destructives interference between the incident and scattered wave field. Again, only symmetric wave modes (S0, SHS0, SHS1, S1, and S2) participated in the scattering procedure,

while no anti-symmetric waves (A0, SHA0, and A1) were converted from the interaction.

### 5.3. A0 mode nonlinear scattering

Fig. 9 shows the WDIC results for the A0 incident wave case at the excitation frequency (250 kHz). It can be observed that the incident A0 wave is scattered as A0 wave and mode converted to both S0 and SHS0 modes. All three possible wave modes participated in the scattering procedure. The scattered A0 mode possessed the highest coefficients, while S0 and SHS0 have very small amplitudes. The most obvious scattering happens along the wave path for A0 and S0 modes, while along 60° direction for SHS0 mode.

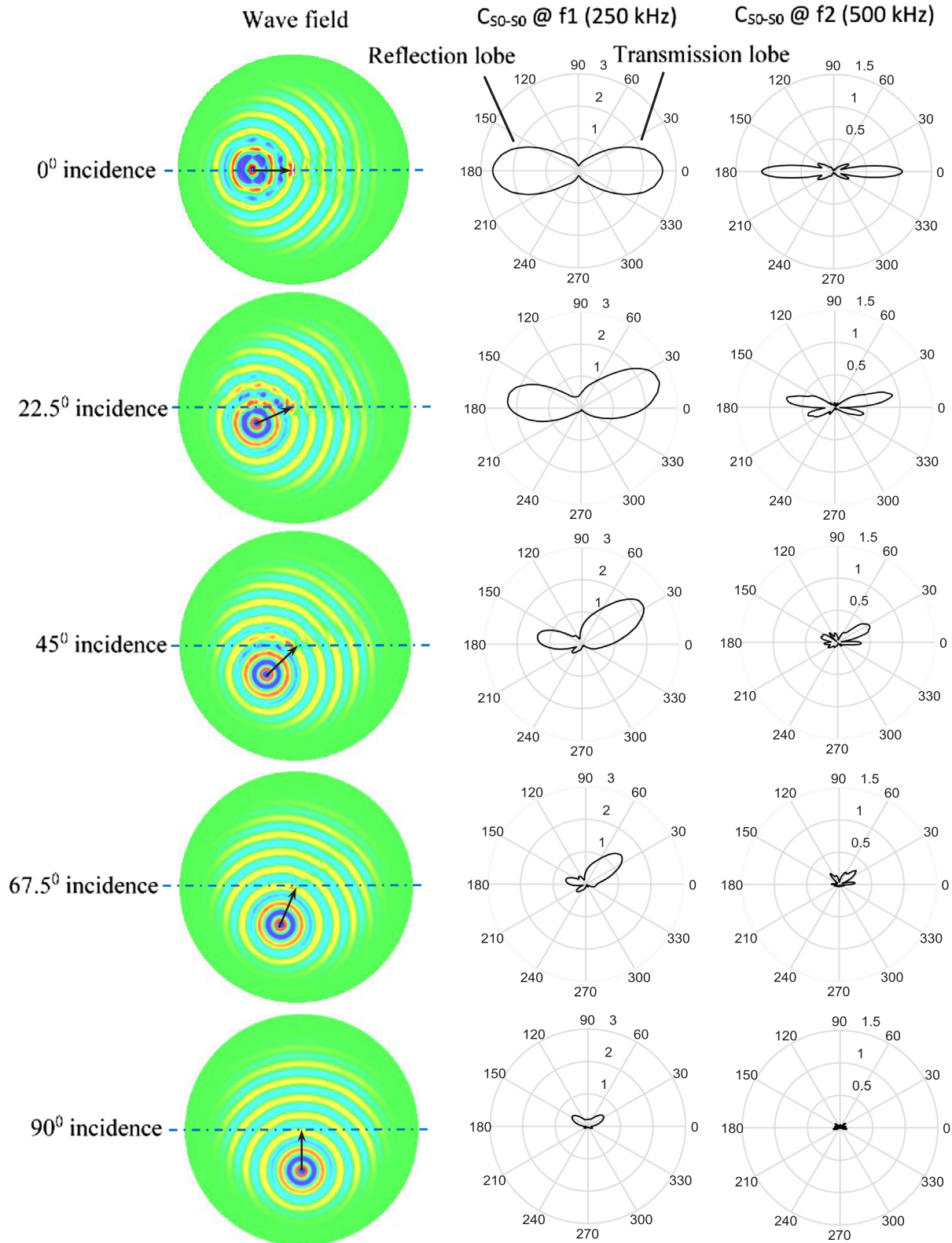At the second harmonic frequency (500 kHz), all five modes (A0, S0,

**Fig. 12.** S0 wave impinging on the crack with various incident angles: wave fields; scattered S0 waves at the fundamental frequency (250 kHz); scattered S0 waves at the second harmonic frequency (500 kHz).

SHS0, SHA0, A1) are found in the scattered wave field as shown in Fig. 10. This is different from the S0 incident wave case, where only symmetric modes (symmetric Lamb modes and symmetric SH modes) are present. Moreover, another interesting phenomenon is that, at the second harmonic frequency, the scattered S0 mode dominates, while A0 mode has a very small scattered amplitude. The backward reflection of S0 wave also shows a much higher amplitude than the forward transmission. This may indicate that a pulse-echo method becomes more sensitive than the pitch-catch method for the detection of second harmonic S0 mode.
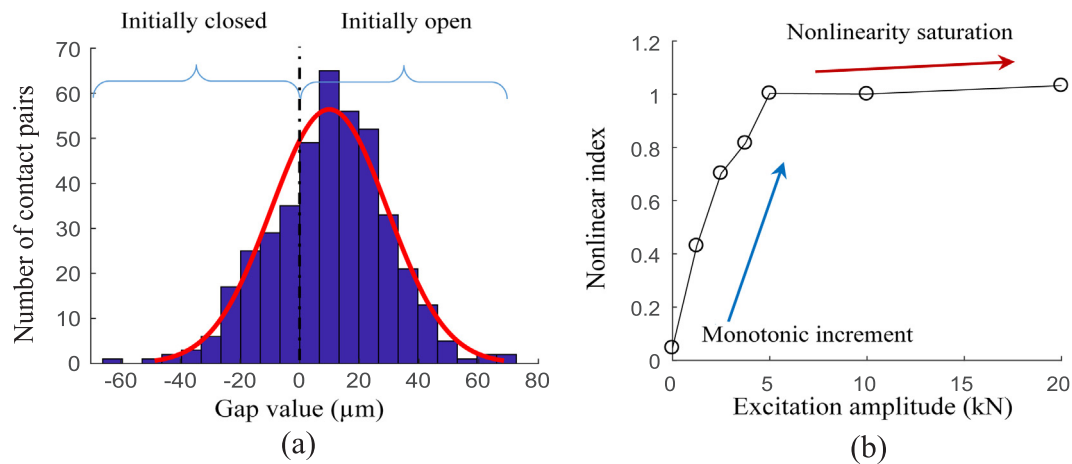
**Fig. 13.** Initial contact pair gap value at the crack interface; amplitude dependent behavior of nonlinear wave damage interactions.

Fig. 11 presents the WDIC results for the A0 incident wave case at the third harmonic frequency (750 kHz), showing that all possible eight wave modes are participating in the nonlinear scattering procedure. The highest amplitude is found in the A0 mode. Both symmetric and antisymmetric Lamb modes present the highest scattering amplitude along the wave path, whereas the SH modes reach their minimum values along such direction. Overall, although higher-order wave modes are present, they possess much smaller amplitudes compared with the fundamental S0 and A0 Lamb modes. And the symmetric and anti-symmetric modes seem to alternate to take the major scattering wave energy at the considered harmonic frequencies. For instance, at the fundamental frequency, the scattered A0 wave has much higher amplitude than both S0 and SHS0 waves. At the second harmonic frequency, however, S0 and SH0 modes show much higher scattering amplitude than the A0, SHA0, and A1 modes. At the third harmonic frequency, A0, SHA0, and A1 modes again possess higher amplitudes than S0, SHS0, SHS1, S1, and S2 modes. Such distinctive alternating participation phenomena as well as the selective mode conversion effect (shown in Figs. 6–8) during the nonlinear wave scattering procedure may provide effective information to detect and diagnose through-thickness breathing cracks in plate-like structures. However, it should be noted that these results are only valid for idealized breathing cracks with smooth, kissing interfaces. When surface roughness and initial crack conditions are considered, the scattering and mode conversion pattern would be more complex.

## 6. Effect of oblique incident angle

The aforementioned example assumed that Lamb waves impinge perpendicularly on the crack. In SHM practice, guided waves may incident the crack profile with an oblique angle, when transmitters misaligned with the crack trajectory normal direction. The scattering pattern of plate guided waves may heavily depend on the incident angle and may substantially influence the SHM system design and signal interpretation for the nonlinear ultrasonic techniques.

In order to investigate such an issue, a case study of S0 mode guided waves impinging on the breathing crack at various incident angles were conducted. Fig. 12 shows the wave propagation and scattering wave field results from the simulation, the scattered S0 wave coefficients at the fundamental frequency (250 kHz), and the scattered S0 wave coefficients at the second harmonic frequency (500 kHz). Of course, the scattering coefficients of other wave modes such as SHS0 and S1 as well as the results at third or even higher harmonic frequencies can also be obtained following the same procedure described in the previous sections. Only the results for S0 modes at the fundamental and second harmonic frequencies are chosen as the representatives of the oblique

incident effect for the sake of presentation brevity. Similar results can be obtained by analyzing the other modes.

Several characteristics of the angular effects are of particular interest and may provide guidelines for nonlinear SHM system design. As the incident angle increases, the scattering amplitudes of S0 waves at both the fundamental and the second harmonic frequencies drop substantially. This indicates that the best actuation and sensing locations are aligned perpendicular to the crack length direction. Furthermore, the transmission scattering lobes become larger than the reflection counterparts as the incident angle grows, which means when the transmitted waves are more indicative of the crack (the transmission and reflection directions are shown in Fig. 12). Another effect is that the maximum transmission and reflection amplitude directivities do not coincide between the fundamental and second harmonic frequencies. Taking the 45° incidence case as an example, the transmission lobe is about 40° at the fundamental frequency but 30° at the second harmonic frequency. The reflection lobe is found at 170° at the fundamental frequency but 160° at the second harmonic frequency. Such skew scattering effect is found to be more sensitive for transmission lobe at the fundamental frequency and the reflection lobe at the second harmonic component.

## 7. Effect of wave amplitude due to initial crack status

In practice, fatigue cracks always present complicated 3-D microscopic rough features, with initial openings and closures along the crack surfaces [58]. These microscopic features may induce threshold and amplitude dependent behaviors, which the idealized "breathing crack" models cannot capture. In the current contact LISA effort, a distributed gap function was introduced to depict the general threshold and amplitude dependent behaviors due to the existence of initial crack opening and closure, details of which can be found in Ref. [54].

In this section, a case study on Lamb wave scattering from a fatigue crack with rough surfaces is presented. The same model setup following the previous sections was adopted, in which there are totally 418 contact pairs. The only difference is that a random normal distribution of initial gap values between the contact pairs are introduced to represent the rough crack surface condition (in practice, such distributions may be obtained from the observation of microscopic images of fatigue cracks). Fig. 13a shows the initial gap value distribution of a partially closed crack, with negative gap values indicating the prestresses caused by initial closures and positive gap values representing initial openings. The peak to peak excitation amplitude was increased from 1 N to 20 kN. The nonlinearity of the sensing signals was measured by the nonlinear index
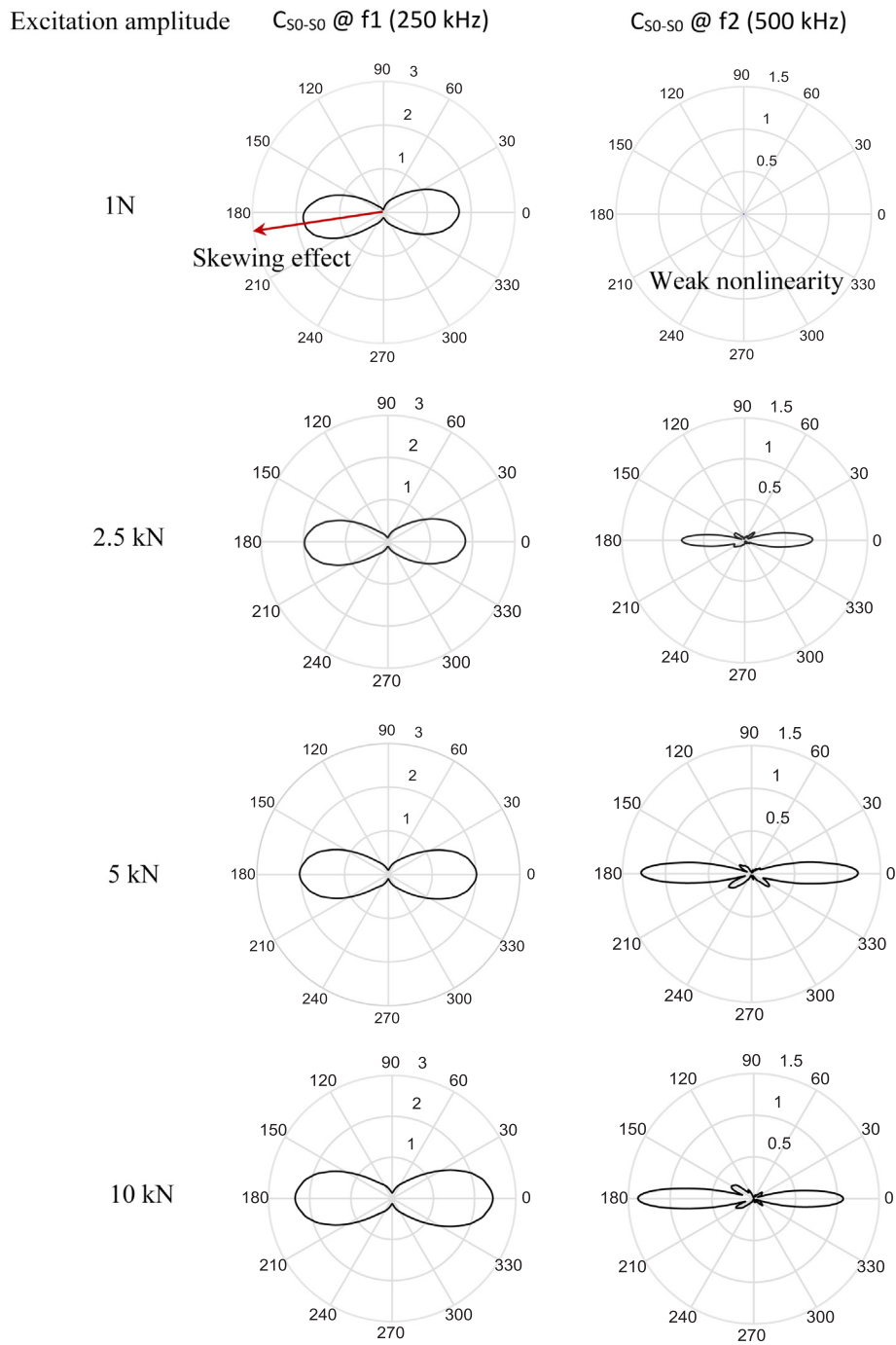
Excitation amplitude    C$_{S0-S0}$ @ f1 (250 kHz)    C$_{S0-S0}$ @ f2 (500 kHz)



**Fig. 14.** S0 wave impinging on a rough crack with various amplitudes: scattered S0 waves at the fundamental frequency (250 kHz); scattered S0 waves at the second harmonic frequency (500 kHz).

$$N_{index} = \sqrt{\frac{A(2f_c) + A(3f_c) + A(4f_c) + A(5f_c)}{A(f_c)}}$$

(10)

where $A(f_c)$, $A(2f_c)$, $A(3f_c)$, $A(4f_c)$, and $A(5f_c)$ denote the spectral amplitude of the fundamental excitation frequency, the second, third, fourth, and fifth higher harmonics. The nonlinearity indices of the sensing signals are traced against the excitation amplitude in Fig. 13b.

It was found that even very small excitation amplitudes would introduce nonlinearity into the sensing signal. The nonlinearity is weak when the excitation amplitude is low, and it increases monotonically with the excitation amplitude until reaching a threshold value, beyond which the nonlinearity asymptotes towards a saturation region, where all the contact pairs are engaged in the contact dynamics.

Fig. 14 presents the scattering coefficient results of S0 wave impinging on a rough crack with various amplitudes. Only scattered S0 waves at the fundamental frequency and the second harmonic are plotted here as the representative. When the excitation amplitude is low, the scattered S0 wave pattern shows a skewing effect, while the nonlinear higher harmonic scattering is rather weak. This is because the low wave amplitude is not sufficient to introduce the clapping mechanism of the nonlinear contact dynamics and the initial openings and closures profile is not symmetric. As the wave amplitude becomes stronger, the scattering coefficients at both the fundamental frequency and the second harmonic increase. The skewing effect disappears as well. The second harmonic scattering coefficient grows more substantially. At the relatively high wave amplitude region, the
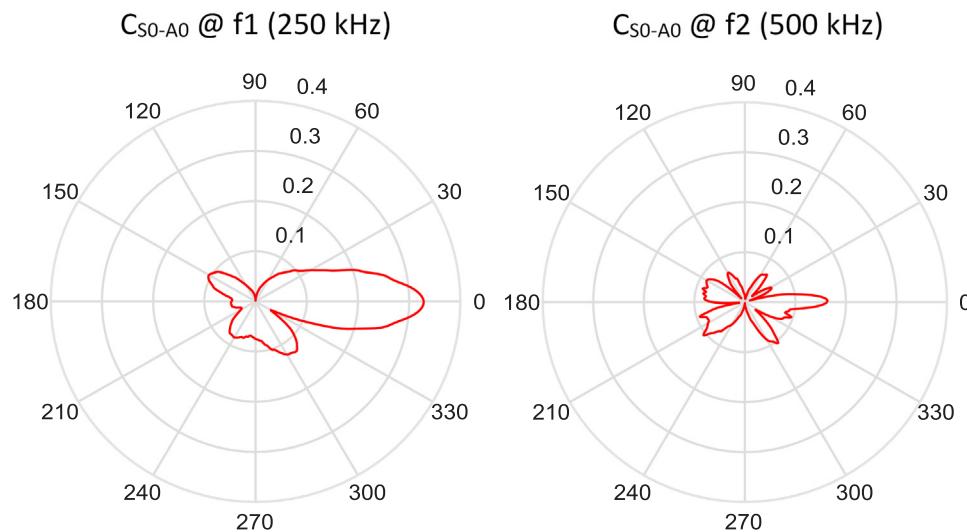
$C_{S0-A0}$ @ f1 (250 kHz)

$C_{S0-A0}$ @ f2 (500 kHz)



**Fig. 15.** S0 wave impinging on a rough crack: scattered A0 waves at the fundamental frequency (250 kHz); scattered A0 waves at the second harmonic frequency (500 kHz).

fundamental S0 wave scattering pattern approaches that in the "breathing crack" case (Fig. 6). The second harmonic scattering pattern also stabilizes. But an interesting phenomenon can be noticed that the forward scattering amplitude may decrease with the increment of excitation amplitude. This is because, for a rough crack surface, A0 wave modes may be converted due to the asymmetry of gap distributions with respect to the mid-plane of the plate thickness. And the scattered energy at the second harmonic may be imparted to other wave modes rather than S0 mode. Fig. 15 presents the mode converted scattered A0 mode from S0 wave incidence on the rough crack with an excitation amplitude of 10 kN. This is quite different compared with the idealized "breathing crack" case results shown in Figs. 6 and 7, where no A0 waves participate in the scattering and mode conversion. Another important feature is that the scattered A0 waves do not follow any symmetric pattern. This is because the initial gap distribution is random.

## 8. Concluding remarks and future work

This article presented an efficient numerical approach to the investigation of nonlinear scattering and mode conversion phenomena of Lamb waves as they interact with breathing cracks. A penalty method and Coulomb friction model was introduced into the Local Interaction Simulation Approach (LISA) formulation, forming an explicit parallelizable solving scheme for Contact Acoustic Nonlinearity (CAN) problems. The small-size LISA model can achieve efficient simulation of linear/nonlinear interaction between guided waves and cracks. The arrangement of excitation and sensing circles allows the investigation of incident waves with arbitrary incident angles and scattering directions.

The mode expansion technique was presented with detailed steps to extract Wave Damage Interaction Coefficients (WDICs) from the small-size LISA model. It involves the Fourier transform of time-domain harmonic LISA solutions. The mode expansion was performed in frequency domain at both fundamental and superharmonic frequencies based on the exact 3-D solution of irradiating waves. This technique is able to consider all the possible wave modes participating in the scattering procedure.

A case study of Lamb wave scattering from a breathing crack was presented first. It was found that the scattering phenomena depends on the incident wave mode. When the S0 impinges on the breathing crack, only symmetric waves are scattered at the fundamental and higher harmonic frequencies. However, when the A0 mode interacts with the breathing crack, all possible wave modes are present in the scattering wave field. Another interesting phenomenon was also observed when

A0 waves impinged on the crack: the symmetric and antisymmetric scattered wave modes showed an alternating behavior, taking turns to carry most of the energy and dominate the scattering at the harmonics.

The effect of oblique incident angles was then investigated. It was found that the incident angle played an important role in the Lamb wave scattering procedure. The scattering amplitude was maximized with a zero degree incident angle and dropped significantly as the incident angle increased. The scattering amplitude directivity differed between the fundamental frequency and the second harmonic.

Considering the rough surface feature of fatigue cracks, initial gap functions were introduced into the LISA model. The effect of wave amplitude during the nonlinear scattering and mode conversion was studied. It was found that the nonlinear higher harmonic scattering pattern depended much on the incident wave amplitude. Low excitation amplitude may result in the skewing effect at the fundamental frequency and may be not sufficient to introduce the scattering phenomena at the superharmonics. The higher harmonic scattering amplitude underwent obvious increment when the wave amplitude became higher. Compared with the "breathing crack" case, the mode conversion and scattering from S0 mode into A0 mode became possible.

This technique shows its potential for studying the nonlinear Lamb wave scattering characteristics at different profiles of damage, which may provide insight for the design of sensor network and damage imaging SHM systems using time reversal techniques based on the scattered wave field.

It should be emphasized again that this article presents the authors' first step of numerical investigation to analyze the nonlinear scattering and mode conversion phenomena at fatigue cracks. It intends to share the efficient numerical modeling scheme and scattering mode directivity quantification approach in a systematic manner. Experimental investigations are being conducted and will be reported in a future paper.

For future work, experiments on Lamb wave scattering at fatigue cracks should be conducted. The rough nature of the cracks should be considered. Special scattering phenomena should be investigated such as nonlinear resonances and possible random scattering directivity patterns. The methodology presented in this study should be applied to improve the time reversal and tomography damage imaging techniques.

## Acknowledgements

## References

[1] K.-Y. Jhang, Nonlinear ultrasonic techniques for nondestructive assessment of micro damage in material: a review, Int. J. Precis. Eng. Manuf. 10 (1) (2009) 123–135.

[2] Z. Su, C. Zhou, M. Hong, L. Cheng, Q. Wang, X. Qing, Acousto-ultrasonics-based fatigue damage characterization: linear versus nonlinear signal features, Mech. Syst. Sig. Process. 45 (1) (2014) 225–239.

[3] D. Dutta, H. Sohn, K.A. Harries, P. Rizzo, A nonlinear acoustic technique for crack detection in metallic structures, Strctural Health Monit. Int. J. 8 (3) (2009) 251–262.

[4] A.N. Norris, C. Vemula, Scattering of flexural waves in thin plates, J. Sound Vib. (1995) 115–125.

[5] C. Vemula, A.N. Norris, Flexural wave propagation and scattering on thin plates using Mindlin theory, Wave Motion 26 (1997) 1–12.

[6] M.K. Hinders, Lamb waves scattering from rivets, Quant. Nondestructive Eval. 15 (1996).

[7] J.C.P. McKeon, M.K. Hinders, Lamb waves scattering from a through hole, J. Sound Vib. (1999) 843–862.

[8] T. Grahn, Lamb wave scattering from a circular partly through-thickness hole in a plate, Wave Motion 37 (1) (2002) 63–80.

[9] C. Wang, F. Chang, Scattering of plate waves by a cylindrical inhomogeneity, J. Sound Vib. 282 (2005) 429–451.

[10] F. Cegla, A. Rohde, M. Veidt, Analytical prediction and experimental measurement for mode conversion and scattering of plate waves at non-symmetric circular blind holes in isotropic plates, Wave Motion 45 (2008) 162–177.

[11] L. Moreau, M. Caleap, A. Velichko, P.D. Wilcox, Scattering of guided waves by through-thickness cavities with irregular shapes, Wave Motion 48 (2011) 586–602.

[12] L. Moreau, M. Caleap, A. Velichko, P.D. Wilcox, Scattering of guided waves by flat-bottomed cavities with irregular shapes, Wave Motion (2012), https://doi.org/10.1016/j.wavemoti.2011.12.004.

[13] B. Poddar, V. Giurgiutiu, Complex modes expansion with vector projection using power flow to simulate Lamb waves scattering from horizontal cracks and disbonds, J. Acoustical Soc. Am. 140 (3) (2016) 2123–2133.

[14] H.S. Lee, Y.Y. Kim, Guided wave scattering analysis for a plate with arbitrary shaped elastic inclusions using the T-matrix method, J. Sound Vib. (2016) 97–111.

[15] D. Alleyne, P. Cawley, The interaction of Lamb waves with defects, IEEE Trans. Ultrason. Ferroelectr. Freq. Control 39 (3) (1992) 381–397.

[16] Y. Cho, D. Hongerholt, J. Rose, Estimation of ultrasonic guided wave mode conversion in a plate with thickness variation, IEEE Trans. Ultrason. Ferroelectr. Frequency Control 47 (3) (2000).

[17] J. Galan, R. Abascal, Boundary element solution for the bidimensional scattering of guided waves in laminated plates, Comput. Struct. 83 (2005) 740–757.

[18] W. Ostachowicz, P. Kudela, M. Krawczuk, A. Zak, Guided Waves in Structures for SHM: The Time-Domain Spectral Element Method, Wiley, West Sussex, UK, 2012.

[19] E. Rahani, T. Kundu, Modeling of transient ultrasonic wave propagation using the distributed point source method, IEEE Trans. Ultrason. Ferroelectr. Freq. Control 58 (10) (2011).

[20] E. Glushkov, N. Glushkova, R. Lammering, A. Eremin, M. Neumann, Lamb wave excitation and propagation in elastic plates with surface obstacles: proper choice of central frequency, Smart Mater. Struct. (2011) 11.

[21] A. Velichko, P. Wilcox, Post-processing of guided wave array data for high resolution pipe inspection, J. Acoust. Soc. Am. 126 (6) (2009) 2973–2982.

[22] A. Velichko, P. Wilcox, A generalized approach for efficient finite element modeling of elastodynamic scattering in two and three dimensions, J. Acoust. Soc. Am. 128 (3) (2010) 1004–1014.

[23] A. Velichko, P. Wilcox, Efficient finite element modeling of elastodynamic scattering from near surface and surfacebreaking defects, in: AIP Conf. Proc. 1335, vol. 59, 2011. doi: https://doi.org/10.1063/1.3591840.

[24] A. Velichko, P. Wilcox, Efficient finite element modeling of elastodynamic scattering with non-reflective boundary conditions, in: AIP Conf. Proc. 1430, vol. 142, 2012. doi: https://doi.org/10.1063/1.4716224.

[25] L. Moreau, A. Velichko, P. Wilcox, Accurate finite element modeling of guided wave scattering from irregular defects, NDT&E Int. 45 (2012) 46–54.

[26] L. Moreau, A. Hunter, A. Velichko, P. Wilcox, 3-D reconstruction f sub-wavelength scatterers from the measurement of scattered fields in elastic waveguides, IEEE Trans. Ultrason. Ferroelectr. Freq. Control 61 (11) (2014) 1864–1879.

[27] S. Hirose, 2-D Scattering by a crack with contact-boundary coditions, Wave Motion 19 (1994) 37–49.

[28] M. Poznic, C. Pecorari, Nonlinear scattering by a partially closed surface breaking crack, in: Review of Quantitatie Nondestructive Evaluation, 2005.

[29] P. Blanloeuil, A. Meziane, A. Norris, C. Bacon, Analytical extension of finite element

[30] solution for computing the nonlinear far field of ultrasonic waves scattered by a closed crack, Wave Motion 66 (2016) 132–146.

[30] P. Blanloeuil, L.R.F. Rose, J. Guinto, M. Veidt, C. Wang, Closed crack imaging using time reversal method based on fundamental and second harmonic scattering, Wave Motion 66 (2016) 156–176.

[31] K. Wang, Z. Su, Analytical modeling of contact acoustic nonlinearity of guided waves and its application to evaluating severity of fatigue damage, in: SPIE Conference Proceeding, Las Vegas, 2016.

[32] K. Wang, Z. Su, A three-dimensional analytical model for interpreting contact acoustic nonlinearity generated by a breathing crack in plate, in: SPIE Conference Proceeding, Portland, 2017.

[33] Y. Shen, V. Giurgiutiu, Predictive modeling of nonlinear wave propagation for structural health monitoring with piezoelectric wafer active sensors, J. Intell. Mater. Syst. Struct. 25 (4) (2013) 506–520.

[34] M. Hafezi, R. Alebrahim, T. Kundu, Peri-ultrasound for modeling linear and nonlinear ultrasonic response, Ultrasonics 80 (2017) 47–57.

[35] M. Hafezi, T. Kundu, Peri-ultrasonic modeling of dynamic response of an interface crack showing wave scattering and crack propgation, J. Nondestructive Eval. Diagnostics Prognostics Eng. Syst. 1 (2018) 1–6.

[36] M. Hafezi, T. Kundu, Peri-ultrasound modeling for surface wave propagation, Ultrasonics (2018) 162–171.

[37] R. Radecki, Z. Su, L. Cheng, P. Packo, W. Staszewski, Modelling nonlinearity of guided ultrasonic waves in fatigued materials using a nonlinear local interaction simulation approach and a spring model, Ultrasonics 84 (2018) 272–289.

[38] S. He, C. Ng, Modelling and analysis of nonlinear guided waves interaction at a breathing crack using time-domain spectral finite element method, Smart Mater. Struct. 26 (2017) 1–15.

[39] Y. Shen, V. Giurgiutiu, Combined analytical FEM approach for efficient simulation of Lamb wave damage detection, Ultrasonics 69 (2016) 116–128.

[40] P. Delsanto, T. Whitcombe, H. Chaskelis, R. Mignogna, Connection machine simulation of ultrasonic wave propagation in materials. I: The one-dimensional case, Wave Motion 16 (1) (1992) 65–80.

[41] P. Delsanto, R. Schechter, H. Chaskelis, R. Mignogna, R. Kline, Connection machine simulation of ultrasonic wave propagation in materials. II: The two-dimensional case, Wave Motion 20 (4) (1994) 295–314.

[42] P. Delsanto, R. Schechter, R. Mignogna, Connection machine simulation of ultrasonic wave propagation in materials III: The three-dimensional case, Wave Motion 26 (4) (1997) 329–339.

[43] B. Lee, W. Staszewski, Modeling of lamb waves for damage detection in metallic strcutures: Part I. Wave propagation, Smart Mater. Struct. 12 (5) (2003) 804–814.

[44] B. Lee, W. Staszewski, Modeling of Lamb waves for damage detection in metallic structures: Part II. Wave interactions with damage, Smart Mater. Struct. 12 (5) (2003) 815–824.

[45] K. Nadella, C. Cesnik, Numerical simulation of wave propagation in composite plates, in: SPIE Smart Structures and NDE, San Diego, 2012.

[46] K. Nadella, C. Cesnik, Local interaction simulation approach for modeling wave propagation in composite structures, CEAS Aeronautical J. 4 (1) (2013) 35–48.

[47] S. Sundararaman, D. Adams, Modeling guided waves for damage identification in isotropic and orthotropic plates using a local interaction simulation approach, J. Vib. Acoust. 130 (4) (2008) 1–16.

[48] K. Nadella, C. Cesnik, Effect of piezoelectric actuator modeling for wave generation in LISA, in: SPIE Smart structures and NDE, San Diego, 2014.

[49] M. Obenchain, K. Nadella, C. Cesnik, Hybrid blobal matrix/local interaction simulation approach for wave propagation in composites, AIAA J. (2014), https://doi.org/10.2514/1.J053101.

[50] Y. Shen, C. Cesnik, Hybrid local FEM/global LISA modeling of damped guided wave propagation in complex composite structures, Smart Mater. Struct. 25 (9) (2016) 1–20.

[51] P. Packo, T. Bielak, A.B. Spencer, T. Uhl, W.J. Staszewski, K. Worden, T. Barszcz, P. Russek, K. Wiatr, Numerical simulations of elastic wave propagation using graphical processing units – comparative study of high-performance computing capabilities, Comput. Methods Appl. Mech. Eng. 290 (1) (2015) 98–126.

[52] P. Kijanka, R. Radecki, P. Packo, W. Staszewski, T. Uhl, GPU-based local interaction simulation approach for simplified temperature effect modelling in Lamb wave propagation used for damage detection, Smart Mater. Struct. 22 (3) (2013) 1–16.

[53] P. Packo, T. Bielak, A. Spencer, W. Staszewski, T. Uhl, K. Worden, Lamb wave propagation modelling and simulation using parallel processing architecture and graphical cards, Smart Mater. Struct. 21 (7) (2012) 1–13.

[54] Y. Shen, C. Cesnik, Modeling of nonlinear interactions between guided waves and fatigue cracks using local interaction simulation approach, Ultrasonics 74 (2017) 106–123.

[55] J. Pettit, A. Walker, P. Cawley, M. Lowe, A stiffness reduction method for efficient absorption of waves at boundaries for use in commercial finite element codes, Ultrasonics 54 (2014) 1868–1879.

[56] Y. Shen, V. Giurgiutiu, Effective non-reflective boundary for Lamb waves: theory, finite element implementation, and applications, Wave Motion 58 (2015) 22–41.

[57] Y. Shen, V. Giurgiutiu, WaveFormRevealer: an analytical framework and predictive tool for the simulation of multi-modal guided wave propagation and interaction with damage, Struct. Health Monit.: Int. J. 13 (5) (2014) 491–511.

[58] H.J. Lim, B. Song, B. Park, H. Sohn, Noncontact fatigue crack visualization using nonlinear ultrasonic modulation, NDT&E Int. 73 (1) (2015) 8–14.